Journal of Computational Physics 228 (2009) 6572–6589

Contents lists available at ScienceDirect

Journal of Computational Physics

journal homepage: www.elsevier.com/locate/jcp

On the HLLC Riemann solver for interface interaction in compressible multi-fluid flow

X.Y. Hu [a,*], N.A. Adams [a], G. Iaccarino [b]

[a] Lehrstuhl für Aerodynamik, Technische Universität München, 85748 Garching, Germany
[b] Center for Turbulence Research, Stanford University, Stanford, CA 94305, United States

ARTICLE INFO

Article history:
Received 11 November 2008
Received in revised form 15 May 2009
Accepted 1 June 2009
Available online 10 June 2009

Keywords:
Multi-fluid flow
Compressible flow
Riemann solver
Roe approximation

ABSTRACT

In this work, the HLLC Riemann solver, which is much more robust, simpler and faster than iterative Riemann solvers, is extended to obtain interface conditions in sharp-interface methods for compressible multi-fluid flows. For interactions with general equations of state and material interfaces, a new generalized Roe average is proposed. For single-phase interactions, this new Roe average does not introduce artificial states and satisfies the U-property exactly. For interactions at material interfaces, the U-property is satisfied by introducing ghost states for the internal energy. A number of numerical tests suggest that the proposed Riemann solver is suitable for general equations of state and has an accuracy comparable to iterative Riemann solvers, while being significantly more robust and efficient.

1. Introduction

In general two main approaches are employed to study the dynamics of compressible multi-fluid flow in an Eulerian description: one is the interface-capturing model in which density and material property vary continuously [12,35,1]; the other is the sharp-interface model in which density and material property are discontinuous across the interface [9,7]. For methods with the sharp-interface model the interaction at the material interface needs to be solved for providing the interface condition.

Simple interface-interaction models may fail due to the lack of accuracy for very strong interactions or large jumps of density and material property [17]. More robust interface methods are obtained when the interface condition is determined by solving a one-dimensional Riemann problem with respect to the normal direction of the interface [17,13]. Many Riemann solvers, with increasing complexity classified as linear approximation, two-shock/rarefaction-wave approximation to fully non-linear, have been developed [31,16]. However, the application of Riemann solvers to the sharp-interface method is limited, due to two essential requirements: one is that the explicit interface states (pressure, velocity) are required; the other is that the solver should be robust and accurate even for strong interface interactions and large jumps of density and material property. Therefore, it is common to construct an exact Riemann solution at the interface, or alternatively to use a two-shock or two-rarefaction approximation for obtaining the interface condition by an iterative root finding algorithm [9,17,13]. Iterative Riemann solvers, however, may encounter difficulties with respect to convergence or due to multiple solutions. The root finding algorithm also can become quite complicated and may cause considerable computational overhead, especially for fluids with a complex equation of state (EOS). On the other hand a linearized Riemann solver is comparably easy to implement and does not require an iterative algorithm, even for fluids with complex EOS.

* Corresponding author.
E-mail address: Xiangyu.Hu@aer.mw.tum.de (X.Y. Hu).

0021-9991/$ - see front matter © 2009 Elsevier Inc. All rights reserved.
doi:10.1016/j.jcp.2009.06.002

Among the linearized Riemann solvers, the HLLC method [11,32], which approximates the solution with two intermediate states enclosed by the estimated minimum- and maximum-speed waves and separated by a contact discontinuity, has proven to be reliable and robust for single-phase flows. For multi-fluid flows, the HLLC solver has also been used in the ALE method [19,33] or the free Lagrangian method [2]. So far, HLLC has been used mainly for calculating the numerical flux within the different fluids and not for solving the interaction at the material interface. The interface condition is still obtained by more complicated iterative Riemann solvers. Since the HLLC solver gives the velocity of a contact discontinuity and an intermediate pressure [32], it provides a suitable basis for constructing material-interface states. There are two important issues related to the application of the HLLC solver for the interaction at material interfaces. First, it is not clear whether the solver in general is sufficiently robust and whether it can reach an accuracy comparable to non-linear Riemann solvers. Second, even though the HLLC solver itself is independent of material properties, the wave-speed estimation requires the values of the Roe-averaged velocity and sound-speed [6,3]. A formulation of Roe averages for general EOS to be used with interface-interaction methods is not yet available.

The Roe-averaged state is obtained from the Roe approximation, where a local linearization is constructed to satisfy the so called U-property for two adjacent states [23]. For a more general EOS than that of an ideal gas, the generalization of the Roe average is not uniquely defined [21]. One possibility is to assume that the averages of internal energy and velocity have the same form. With this assumption Glaister [8] derived the Roe-average state which satisfies the U-property exactly. However, the artificially introduced intermediate density and internal energy may not be admissible for some EOS. To avoid artificial states, Liou et al. [18] suggested to use extra intermediate derivatives from the average of density and pressure with a more involved formulation. Shyue [27] developed the Roe average for Mie–Grüneisen-type EOSs. The Grüneisen coefficient was assumed to have the same average form as the velocity. However, since this method satisfies the U-property only approximately, it may cause problems for cases with very large density and pressure ratios. When this method is applied for an interaction at material interfaces, all average and adjacent states are assumed to be described by one single EOS, which may be an oversimplification as the EOS of the different materials generally are not related and may produce non-single-valued states.

In this paper, an HLLC solver is developed for the interaction at material interfaces. An extension of the Roe average for a generalized EOS is proposed for the estimation of the minimum and maximum wave speeds. Unlike the method proposed by Liou et al. [18] and Shyue [27], the method is simple and satisfies the U-property exactly for single-phase interactions. Unlike the method of Glaister [8], it does not introduce artificial states and predicts averages directly from the adjacent states. For interactions at material interfaces, unlike the method of Shyue [27], the method does not assume the same EOS for the average and adjacent states. With an introduction of proper ghost states for internal energy, the U-property can be satisfied for the separate materials. To test the robustness and accuracy of the HLLC solver for compressible multi-fluid problems, a number of one- and two-dimensional tests are carried out and results are compared to analytical and previous results.

2. Method

Assuming the fluid to be inviscid and compressible the governing equation of the flow can be written as a system of conservation laws

$$\frac{\partial \mathbf{U}}{\partial t} + \nabla \cdot \mathbf{F} = 0 \quad \text{on} \quad \Omega, \tag{1}$$

where $\mathbf{U}$ is the density of the conserved quantities of mass, momentum and total energy, and $\mathbf{F}$ represents the corresponding flux functions. When a material interface $\Gamma(t)$ separates the domain Ω into two parts, the fluid states in the left and the right sub-domains $\Omega_l(t)$ and $\Omega_r(t)$ are described by different EOS. The evolution of the interface, and the exchange of momentum and energy across the interface are determined by the interface condition, which is obtained by solving a one-dimensional, two-material Riemann problem

$$\mathscr{R}(\mathbf{U}_l, \mathbf{U}_r) = 0 \quad \text{on } \Gamma(t), \tag{2}$$

where $\mathbf{U}_l$ and $\mathbf{U}_r$ represent the left and right states in the normal direction [14]. Neglecting the friction contribution in the tangential direction (inviscid), the one-dimensional governing equation in the normal direction can be written as

$$\mathbf{U}_t + \mathbf{F}(\mathbf{U})_x = 0, \tag{3}$$

where $\mathbf{U} = (\rho, \rho u, E)^T$ and $\mathbf{F}(\mathbf{U}) = (\rho u, p + \rho u^2, u(E+p))^T$. Furthermore, together with $E = \rho e + \frac{1}{2}\rho u^2$ and $H = e + \frac{p}{\rho} + \frac{1}{2}u^2$, where ρ, p, e and H represent the density, pressure, specific internal energy, enthalpy, respectively, and u and E represent the velocity normal to the interface and the total energy, respectively. We assume a general EOS of the form

$$p = p(\rho, e). \tag{4}$$

Note that there are usually different formulations for $p(\rho, e)$ across the interface. The sound speed c is given by

$$c^2 = \left.\frac{\partial p}{\partial \rho}\right|_e + \frac{p}{\rho^2}\left.\frac{\partial p}{\partial e}\right|_\rho = \Psi + \Gamma\frac{p}{\rho}, \tag{5}$$

where $\Gamma = \frac{1}{\rho}\frac{\partial p}{\partial e}\Big|_{\rho}$, which is the Grüneisen coefficient, and $\Psi = \frac{\partial p}{\partial \rho}\Big|_{e}$ determine the material properties. Eqs. (3) and (4) lead to the following expression of the Jacobian

$$\frac{\partial F}{\partial U} = \begin{pmatrix} 0 & 1 & 0 \\ \Gamma\left(\frac{1}{2}u^2 - e\right) + \Psi - u^2 & u(2-\Gamma) & \Gamma \\ u\left[\Gamma\left(\frac{1}{2}u^2 - e\right) + \Psi - H\right] & H - u^2\Gamma & u(\Gamma+1) \end{pmatrix}. \tag{6}$$

The eigenvalues λ_i and corresponding right eigenvectors $\mathbf{r}_i$ are then found to be

$$\lambda_1 = u + c, \quad \lambda_2 = u - c, \quad \lambda_3 = u, \tag{7}$$

and

$$\begin{aligned} \mathbf{r}_1 &= (1, u + c, H + uc)^T, \\ \mathbf{r}_2 &= (1, u - c, H - uc)^T, \\ \mathbf{r}_3 &= \left(1, u, \frac{1}{2}u^2 + e - \frac{\Psi}{\Gamma}\right)^T. \end{aligned} \tag{8}$$

2.1. The HLLC solver

The Harten, Lax, and van Leer with contact restoration (HLLC) Riemann solver [11,32] approximates the exact Riemann solution by two waves, one with the smallest and the other with the largest wave speed, denoted as b_l and b_r, respectively, and a contact wave whose speed is denoted as b_m, as shown in Fig. 1. There are two intermediate states, $(\rho_l^*, u_l^*, p_l^*), (\rho_r^*, u_r^*, p_r^*)$, separated by the contact wave. By assuming that the contact wave and intermediate state have the relations

$$b_m = u_l^* = u_r^* = u^*, \quad p_l^* = p_r^* = p^*, \tag{9}$$

Toro et al. [32] obtain the contact wave velocity

$$u^* = \frac{\rho_r u_r(b_r - u_r) + \rho_l u_l(u_l - b_l) + p_l - p_r}{\rho_r(b_r - u_r) + \rho_l(u_l - b_l)}. \tag{10}$$

and the intermediate pressure

$$p^* = p_l + \rho_l(u_l - b_l)(u_l - u^*) = p_r + \rho_r(b_r - u_r)(u^* - u_r). \tag{11}$$

As we consider the two-material Riemann problem, Eq. (2), the interface condition is given by the contact-wave velocity u^* and the intermediate pressure p^*. We estimate the wave-speeds, b_l and b_r, by

$$b_l = \min[u_l - c_l, \tilde{u} - \tilde{c}], \quad b_r = \max[\tilde{u} + \tilde{c}, u_r + c_r], \tag{12}$$

where c is the sound speed, and the tilde ~ indicates Roe-averaged values [6,3]. In the next section, we propose an extension of the Roe average for generalized EOS.

2.2. A generalized Roe average

Following Roe [23] and Glaister [8] we consider the algebraic problem of finding average eigenvalues $\tilde{\lambda}_i$ and corresponding right eigenvectors $\tilde{\mathbf{r}}_i$, such that the U-property

$$\Delta\mathbf{U} = \sum_{j=1}^{3} \tilde{\alpha}_i \tilde{\mathbf{r}}_i, \quad \Delta\mathbf{F} = \sum_{j=1}^{3} \tilde{\lambda}_i \tilde{\alpha}_i \tilde{\mathbf{r}}_i, \tag{13}$$

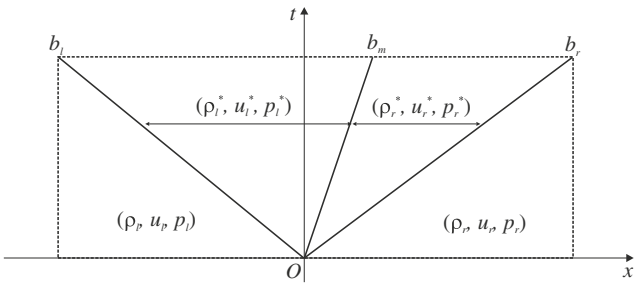

Fig. 1. Schematic of the HLLC approximate Riemann problem.

where $\tilde{\alpha}_i$ are coefficients and $\Delta(\cdot) = (\cdot)_r - (\cdot)_l$, holds exactly for two arbitrary adjacent states $\mathbf{U}_l$ and $\mathbf{U}_r$. Specifically, we seek averages $\tilde{\rho}, \tilde{u}, \widetilde{H}, \tilde{e}, \widetilde{\Gamma}$ and $\widetilde{\Psi}$ in

$$\tilde{\lambda}_1 = \tilde{u} + \tilde{c}, \quad \tilde{\lambda}_2 = \tilde{u} - \tilde{c}, \quad \tilde{\lambda}_3 = \tilde{u}, \tag{14}$$

$$\tilde{\mathbf{r}}_1 = (1, \tilde{u} + \tilde{c}, \widetilde{H} + \tilde{u}\tilde{c})^T, \quad \tilde{\alpha}_1 = \frac{1}{2\tilde{c}^2}(\Delta p + \tilde{\rho}\tilde{c}\Delta u),$$

$$\tilde{\mathbf{r}}_2 = (1, \tilde{u} - \tilde{c}, \widetilde{H} - \tilde{u}\tilde{c})^T, \quad \tilde{\alpha}_2 = \frac{1}{2\tilde{c}^2}(\Delta p - \tilde{\rho}\tilde{c}\Delta u), \tag{15}$$

$$\tilde{\mathbf{r}}_3 = \left(1, \tilde{u}, \frac{1}{2}\tilde{u}^2 + \tilde{e} - \frac{\widetilde{\Psi}}{\widetilde{\Gamma}}\right)^T, \quad \tilde{\alpha}_3 = \Delta\rho - \frac{\Delta p}{\tilde{c}^2}$$

and

$$\tilde{c}^2 = \widetilde{\Psi} + \widetilde{\Gamma}\widetilde{\left(\frac{p}{\rho}\right)}. \tag{16}$$

Following the approach of Glaister [8] the averages $\tilde{\rho}, \tilde{u}$ and $\widetilde{H}$ can be obtained from

$$\tilde{\rho} = \sqrt{\rho_l \rho_r}, \quad \tilde{f} = \mu(f) = \frac{\sqrt{\rho_l} f_l + \sqrt{\rho_r} f_r}{\sqrt{\rho_l} + \sqrt{\rho_r}}, \quad f = u, H \tag{17}$$

and

$$\widetilde{\left(\frac{p}{\rho}\right)} = \mu\left(\frac{p}{\rho}\right) + \frac{1}{2}\left(\frac{u_r - u_l}{\sqrt{\rho_l} + \sqrt{\rho_r}}\right)^2. \tag{18}$$

One can find that the average pressure $\tilde{p} = \tilde{\rho}\widetilde{\left(\frac{p}{\rho}\right)}$ only depends on the densities, pressures and velocities of the adjacent states. On substituting Eq. (17) into Eq. (13) one obtains a condition for pressure difference

$$\Delta p = \widetilde{\Psi}\Delta\rho + \widetilde{\Gamma}[\Delta(\rho e) - \tilde{e}\Delta\rho]. \tag{19}$$

This relation is equivalent to that of Glaister [8] but has a different form. Next, we consider this condition for single-phase and two-material interactions.

2.2.1. Single-phase interaction

In a single phase all the states are described by the same EOS and hence are single-valued, i.e., the states with the same density and internal energy have the same pressure. Therefore, it is straightforward to assume a linear approximation between the average state and the adjacent states, i.e.

$$\Delta p = \widetilde{\Psi}\Delta\rho + \widetilde{\Gamma}\tilde{\rho}\Delta e. \tag{20}$$

On substitution of Eq. (20) into Eq. (19) one obtains the average of the internal energy $\tilde{e} = \mu(e)$, which has the same form as that of Glaister [8]. With $\widetilde{\Psi}$ and $\widetilde{\Gamma}$, there are two unknowns in Eq. (20). A simple solution is to assume that one of them has the same average form as velocity and just calculate the other from Eq. (20). However, this simple way may fail if the variation of density, or internal energy vanishes. For example, when one assumes $\widetilde{\Psi} = \mu(\Psi)$ and calculates $\widetilde{\Gamma} = \widetilde{\Gamma}_{\Delta e} = \frac{\Delta p - \mu(\Psi)\Delta\rho}{\tilde{\rho}\Delta e}$, $\widetilde{\Gamma}$ becomes undefined if $\Delta e = 0$. A similar situation occurs when one assumes $\widetilde{\Gamma} = \mu(\Gamma)$ and calculates $\widetilde{\Psi} = \widetilde{\Psi}_{\Delta\rho} = \frac{\Delta p - \mu(\Gamma)\tilde{\rho}\Delta e}{\Delta\rho}$, which is undefined for $\Delta\rho = 0$. Note, however, that the singularities can be removed if it is assumed that $\widetilde{\Gamma} = \mu(\Gamma)$ for $\Delta e = 0$ and $\widetilde{\Psi} = \mu(\Psi)$ for $\Delta\rho = 0$. Hence, $\widetilde{\Psi}$ and $\widetilde{\Gamma}$ can be generalized by the following weighted averages

$$\widetilde{\Psi} = \frac{\mu(\Psi)(w_e + \epsilon) + \widetilde{\Psi}_{\Delta\rho} w_\rho}{w_\rho + w_e + \epsilon}, \quad \widetilde{\Gamma} = \frac{\mu(\Gamma)(w_\rho + \epsilon) + \widetilde{\Gamma}_{\Delta e} w_e}{w_\rho + w_e + \epsilon}. \tag{21}$$

Here, $w_\rho = \left(\frac{\Delta\rho}{\rho}\right)^2$ and $w_e = \left(\frac{\Delta e}{e}\right)^2$, and ϵ is a small positive number. The averages in Eq. (21) are consistent with the U-property. Specifically, for an ideal gas, $p = \Gamma\rho e, \Gamma = \gamma - 1$, Eq. (21) gives $\widetilde{\Gamma} = \Gamma$ and $\widetilde{\Psi} = \Gamma\mu(e)$, and recovers the original approximation of Roe [23].

2.2.2. Two-material interaction

If the two adjacent states are described by two different EOS then they are not necessarily single-valued, that is, they may have the same density and pressure but different internal energy. Therefore, it may be not possible to satisfy the U-property given by Eq. (19). On the other hand, the linear relation in Eq. (20) becomes questionable since the two EOSs usually are not related. One possible way is to assume that the U-property is satisfied separately for the left and right materials by

introducing appropriate ghost states for each fluid on the opposite side of the interface. The former Eq. (19) now becomes for the left and right side of the interface

$$\begin{aligned}\Delta p &= \widetilde{\Psi}\Delta\rho + \widetilde{\Gamma}[(\rho_r e_r - \rho_l e_l^g) - \tilde{e}_l\Delta\rho],\\ \Delta p &= \widetilde{\Psi}\Delta\rho + \widetilde{\Gamma}[(\rho_r e_r^g - \rho_l e_l) - \tilde{e}_r\Delta\rho],\end{aligned} \tag{22}$$

respectively. Here, e_l^g and e_r^g are the two ghost states of internal energy, and $\tilde{e}_l$ and $\tilde{e}_r$ are the two corresponding averages. Note that, since the average velocity and the average pressure are independent of the internal energy distribution, they are not influenced by the ghost states. Subsequently, the linear relation of Eq. (20) can be given separately for each side of the interface

$$\Delta p = \widetilde{\Psi}\Delta\rho + \widetilde{\Gamma}\tilde{\rho}(e_r^g - e_l), \quad \Delta p = \widetilde{\Psi}\Delta\rho + \widetilde{\Gamma}\tilde{\rho}(e_r - e_l^g), \tag{23}$$

respectively. By comparing Eqs. (22) and (23), and using Eq. (17), the averages related to the internal energy are obtained as

$$\tilde{f}_l = \frac{\sqrt{\rho_l}f_l + \sqrt{\rho_r}f_r^g}{\sqrt{\rho_l}+\sqrt{\rho_r}}, \quad \tilde{f}_r = \frac{\sqrt{\rho_l}f_l^g + \sqrt{\rho_r}f_r}{\sqrt{\rho_l}+\sqrt{\rho_r}}, \quad f = e, H, \tag{24}$$

where $H_l^g = \frac{p_l}{\rho_l} + \frac{1}{2}u_l^2 + e_l^g$ and $H_r^g = \frac{p_r}{\rho_r} + \frac{1}{2}u_r^2 + e_r^g$ are the corresponding ghost enthalpies. Then the averages $\widetilde{\Psi}$ and $\widetilde{\Gamma}$, and the ghost states e_l^g and e_r^g are determined by the two equations of Eq. (23). Since there are four unknowns, a straightforward solution similar to that for the single-phase interaction is to assume

$$\widetilde{\Gamma} = \mu(\Gamma) \quad \text{and} \quad \widetilde{\Psi} = \mu(\Psi), \tag{25}$$

and calculate the two ghost states from Eq. (23)

$$e_r^g = e_l + \frac{\Delta p - \widetilde{\Psi}\Delta\rho}{\widetilde{\Gamma}\tilde{\rho}} \quad \text{and} \quad e_l^g = e_r - \frac{\Delta p - \widetilde{\Psi}\Delta\rho}{\widetilde{\Gamma}\tilde{\rho}}. \tag{26}$$

Eq. (25) suggests that, even though each fluid has a different EOS, the material properties at the averaged state have the same average form as the velocity. Therefore, the average sound speeds for the left and right materials are also the same. Note that when vacuum is considered the average simply gives the state of the non-vacuum side as the averaged state. Also note that, since the two-material Roe average in this paper is used only to obtain the average of velocity and sound speed, the average in Eq. (24) are not required for computation.

3. Numerical examples

In the following numerical examples are provided to illustrate the potential of the proposed HLLC solver for material-interface interactions. For all test cases we employ as underlying discrete scheme a conservative-interface method for multi-fluid problems [14] (see Appendix A), in which the material interface is tracked by a level set [22], and the underlying finite-volume scheme operating on a Cartesian grid is modified by considering computational cells being cut by the interface. Specifically, the interface velocity and interface pressure, obtained by the above Riemann solver, are used to calculate the flux of momentum and energy across the interface patches in cut cells. While the flow field of individual fluids is solved by the single-phase characteristic 5th-order WENO-LLF scheme [15] and a 3rd-order TVD Runge–Kutta scheme for time integration [26], the single-phase Roe approximation developed in this paper is used for the characteristic decomposition at the cell faces. To decrease the over-dissipation in smooth regions caused by the WENO limiter, the anti-diffusion technique given in Borges et al. [4] is used (see Appendix B). We shall denote"M-HLLC" results obtained by the present HLLC solver, and"TR" results obtained by the two-rarefaction-wave Riemann solver [24,13]. If not mentioned otherwise, for one-dimensional examples, the number of grid points is 200 and the reference exact solution, if given, is sampled on 1000 grid points. All the computations, if not mentioned otherwise, are carried out with a CFL number of 0.6.

3.1. Shock-tube problems (I)

Two two-material shock-tube problems of two gases modeled by ideal-gas EOSs with different γ and with very different shock strengths are considered. In Case I-A, which is taken from Fedkiw et al. [7], Hu and Khoo [13] and Hu et al. [14], the shock is moderately strong. The initial condition is

$$(\rho, u, p, \gamma) = \begin{cases}(1, 0, 1, 1.4) & \text{if } 0 < x < 0.5\\ (0.125, 0, 0.1, 1.667) & \text{if } 1 > x > 0.5\end{cases}, \tag{27}$$

and the final time is $t = 0.15$. In Case I-B, which is taken from Abgrall and Karni [34], and Hu and Khoo [13], the shock is very strong. The initial condition is

$$(\rho, u, p, \gamma) = \begin{cases}(1, 0, 500, 1.4) & \text{if } 0 < x < 0.5\\ (1, 0, 0.2, 1.667) & \text{if } 1 > x > 0.5\end{cases}, \tag{28}$$

and the final time is $t = 0.015$. Fig. 2 gives the computed velocity and density profiles, which shows good agreement with the exact solutions. Note that there is no notable difference between the results obtained with the M-HLLC solver and the TR solver. The performance analysis of Case I-A shows that computational time of the TR solver and the M-HLLC solver are both very small (less than 0.005%) compared to total computational time.

3.2. Shock–interface interaction (II)

Three problems on strong shock–interface interaction are considered. The fluids are modeled with ideal-gas EOS with different γ. In Case II-A, which is taken from Liu et al. [17], a strong rarefaction wave is produced when the shock wave impinges on the material interface. The initial condition is

$$(\rho, u, p, \gamma) = \begin{cases} (3.984, 27.355, 1000, 1.667) & \text{if } 0 < x < 0.2 \\ (0.1, 0, 1, 1.667) & \text{if } 1 > x > 0.2 \end{cases}, \tag{29}$$

and the final time is $t = 0.01$. In Case II-B, which is also taken from Liu et al. [17], a strong transmitted shock wave is produced when the shock wave impinges on the material interface. The initial condition is

$$(\rho, u, p, \gamma) = \begin{cases} (0.384, 27.077, 100, 1.667) & \text{if } 0 < x < 0.3 \\ (1.0, 0, 1, 1.667) & \text{if } 1 > x > 0.3 \end{cases}, \tag{30}$$

and the final time is $t = 0.03$. Case II-C is a two-blast-wave interaction problem, which is taken from Woodward and Colella [34] and Hu and Khoo [13]. This is an one-phase problem and the two contact discontinuities are located near the ends of the domain. The initial condition is

$$(\rho, u, p, \gamma) = \begin{cases} (1, 0, 1000, 1.4) & \text{if } 0 < x < 0.1 \\ (1, 0, 0.01, 1.4) & \text{if } 0.1 < x < 0.9 \\ (1, 0, 100, 1.4) & \text{if } 1 > x > 0.9 \end{cases}, \tag{31}$$

and reflective boundary condition is applied at both $x = 0$ and $x = 1$. We examine the numerical solutions on 400 grid points, and the reference solution is a high-resolution numerical solution on 1600 grid points by the TR solver.

Fig. 3 gives the computed velocity and density profiles. Again, good agreement with the reference solutions is observed. Note that for Case II-A the TR solver needs a smaller time-step (CFL = 0.3) to obtain a stable solution. Also note that for Case

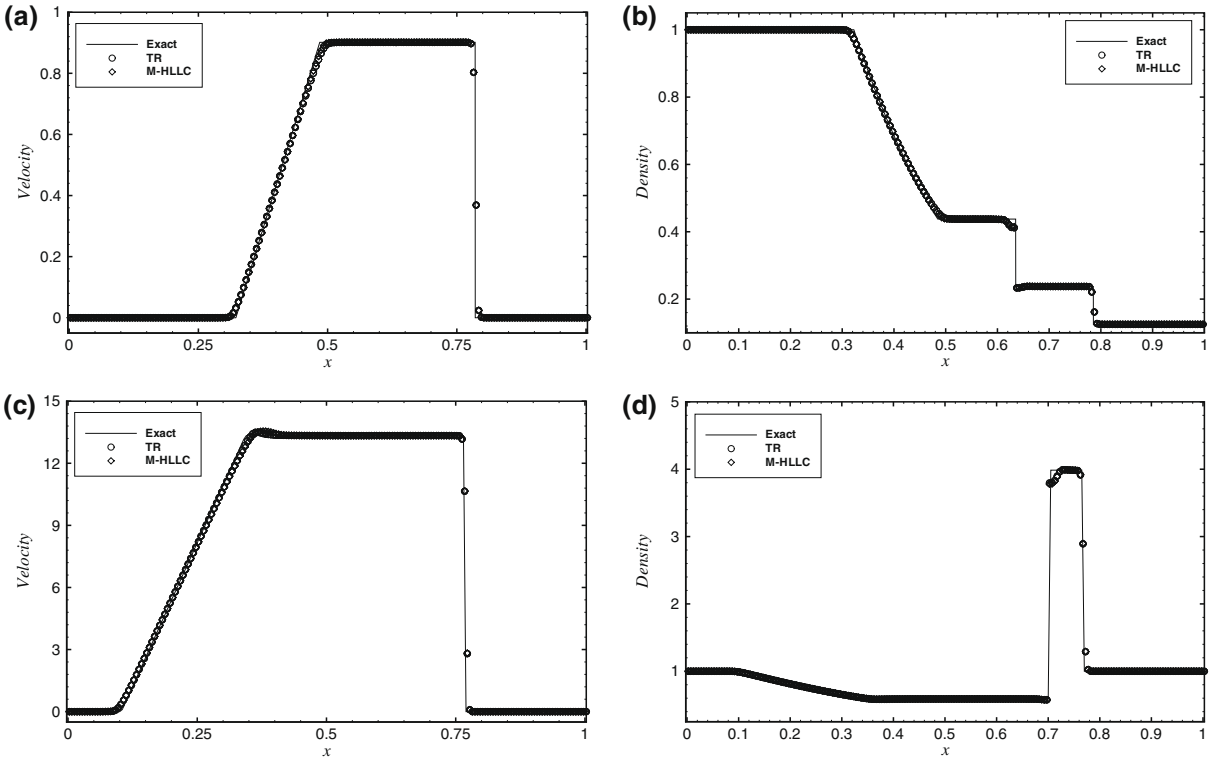

Fig. 2. Shock-tube problems: Case I-A (a) and (b); Case I-B (c) and (d).

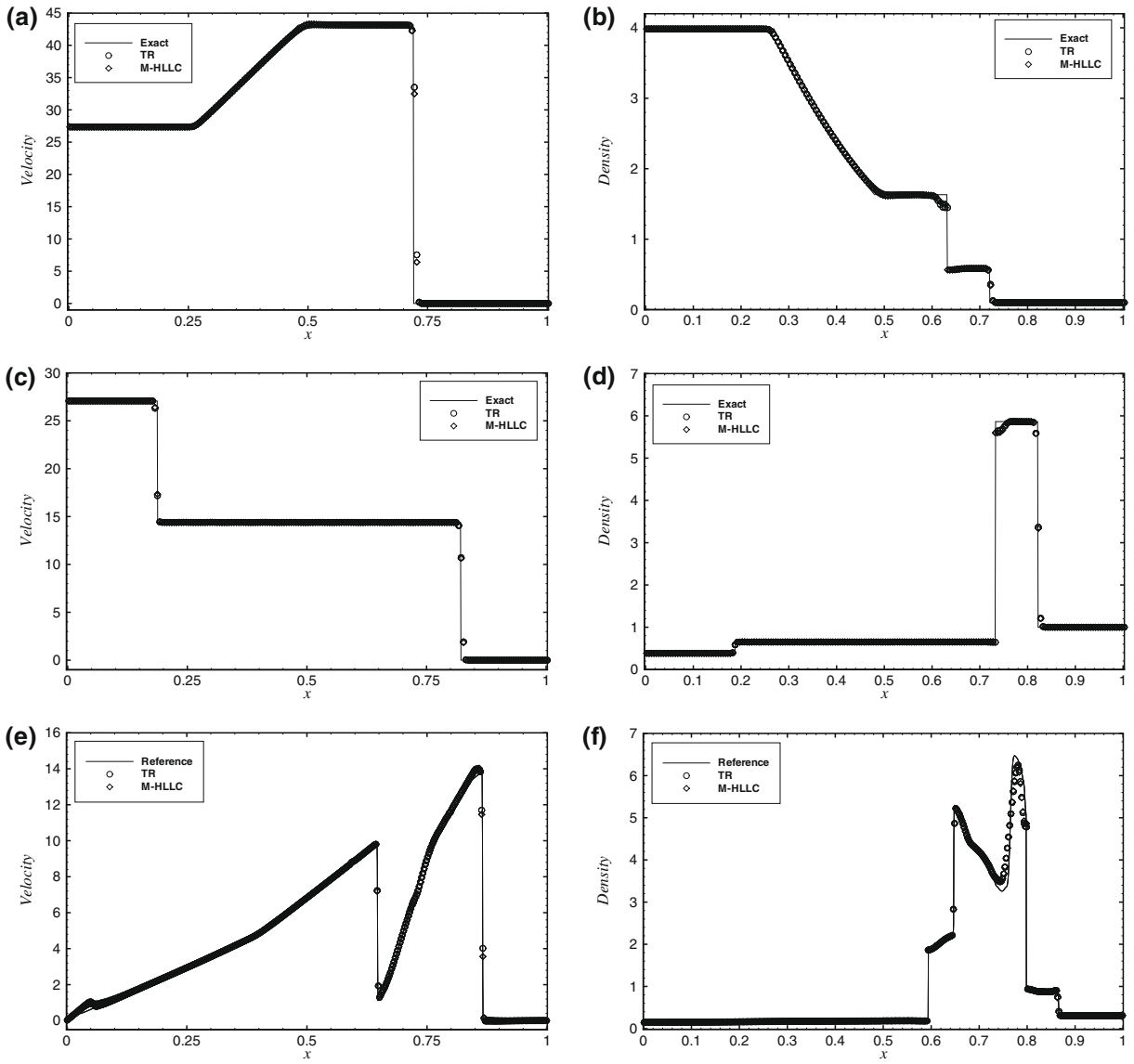

Fig. 3. Shock–interface interaction: Case II-A (a) and (b); Case II-B (c) and (d); Case II-C (e) and (f).

II-C, a comparison with the results on the same grid calculated by the non-conservative method in Hu and Khoo [13] (their Figs. 10 and 11 shows that the present conservative method predicts a more accurate density profile, but it also produces a small"glitch" close to the left boundary. This glitch can be tracked back to an velocity overshoot produced in the solution of the left shock tube problem. Since this overshoot decreases it amplitude with grid size, the"glitch" is not obvious in fine-resolution results. For the results of Hu and Khoo [13] the overshoot is suppressed by the employed entropy-fix technique [7]. Here, we prefer not to use this entropy fix since it may results considerable conservation violation which is undesirable for multi-fluid problems. The performance analysis of Case II-C shows that while the TR solver takes about 0.04% of the total computational time, the computational time of the M-HLLC solver is negligible (less than 0.005%). Note that the TR solver needs considerable more iterations for determining the interface condition since the interface interaction in Case II-C is much stronger than that in Case I-A.

3.3. Interaction with water (III)

We consider two problems with gas-water interaction, in which the gases are modeled with an ideal-gas EOS and water is modeled with Tait's EOS, $p = B\left(\frac{\rho}{\rho_0}\right)^{\gamma} - B + A$, where $\gamma = 7.15$. The non-dimensional parameters are $B = 3310, A = 1$ and $\rho_0 = 1$ with respect to the state of water at 1 atmosphere and length scale 1 m. Case III-A, taken from Hu and Khoo [13],

is a gas-water shock-tube problem, in which the high-pressure gas expands slowly compared to the transmitted and reflected wave front speeds. The initial condition is given as

$$(\rho,u,p,\gamma)=\begin{cases}(0.01,0,1000,2) & \text{if } 0<x<0.5\\ (1,0,1,7.15) & \text{if } 1>x>0.5\end{cases}, \tag{32}$$

and the final time is $t=0.008$. Case III-B, taken from Liu et al. [17] and Hu et al. [14], is an air–bubble-collapse problem in one dimension. The initial condition is

$$(\rho,u,p,\gamma)=\begin{cases}(1.0376,6.0151,1000,7.15) & \text{if } 0<x<0.7\\ (0.001,0,1,1.4) & \text{if } 1>x>0.7\end{cases}, \tag{33}$$

and the final time is $t=0.003$.

Fig. 4 gives the computed velocity, density profiles, which show a good agreement with the exact solutions. There is no notable difference between the results obtained with the M-HLLC solver and the TR solver. Also note that the present results predict sharper wave fronts than those in Hu and Khoo [13] and Hu et al. [14] because of the employed anti-diffusion technique.

3.4. Explosive driving and high-speed impact (IV)

Three problems on explosive driving and high-speed impact are considered. The explosive is modeled with the Jones–Wilkins–Lee (JWL) EOS,

$$p=A_0\exp\left(\frac{-R_1\rho_o}{\rho}\right)\left(1-\frac{\rho}{R_1\rho_0}\right)+B_0\exp\left(\frac{-R_2\rho_o}{\rho}\right)\left(1-\frac{\rho}{R_2\rho_0}\right)+\Gamma_0\rho(e+e_0)$$

where $A_0,B_0,R_1,R_2,\rho_0,e_0$ and Γ_0 are constant coefficients. The impacting materials are modeled by a Mie–Grüneisen EOS,

$$p(\rho,e)=p_{ref}+\Gamma(\rho)\rho(e-e_{ref})$$

where $p_{ref}=\rho_0c_0^2\eta/(1-s\eta)^2,\eta=1-\rho_0/\rho,\Gamma(\rho)=\Gamma_0\rho_0/\rho$ and $e_{ref}=0.5p_{ref}\eta/\rho_0$. Here ρ_0,c_0,s,Γ_0 are constant coefficients. The dimensional reference values are 1000 kg/m^3, 1 GPa and 1 m. The TR solver becomes complicated for these types of EOS, and is not available to us. For this reason, the reference solution is taken from a high-resolution M-HLLC computation with 1600 grid points. Case IV-A, which is taken from Saurel and Abgrall [25] and Shyue [27], involves the interaction

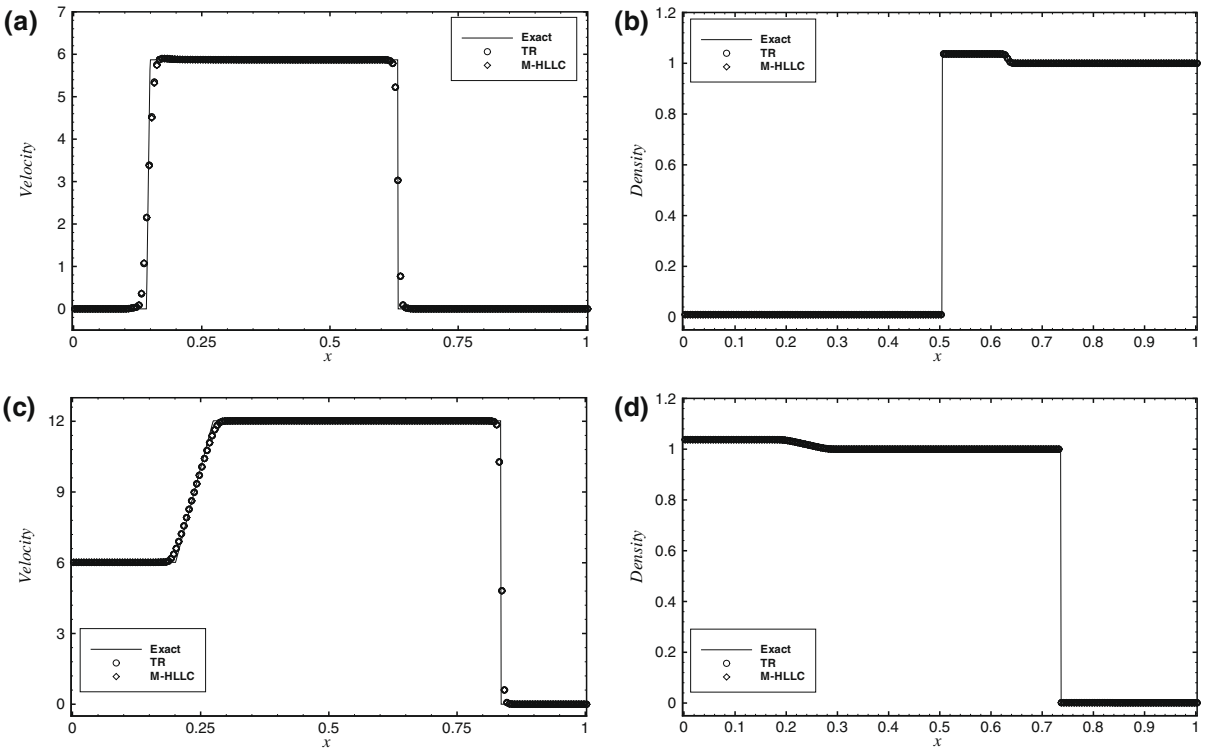

Fig. 4. Interaction with water: Case III-A (a) and (b); Case III-B (c) and (d).

between the detonation products of TNT explosive with a copper plate. The EOS coefficients of the detonation products and the copper plate are $(\Gamma,\rho_0,A_0,B_0,R_1,R_2,e_0)=(0.25,1.84,854.5,20.5,4.6,1.35,8.15)$ and $(\Gamma_0,\rho_0,c_0,s)=(1.96,8.924,3.91,1.51)$, respectively. The initial condition is

$$(\rho,u,p)=\begin{cases}(2.48537,0.0,37) & \text{if } 0<x<0.5\\ (8.924,0,0) & \text{if } 1>x>0.5\end{cases} \tag{34}$$

and the final time is $t=0.06$. Case IV-B, which is taken form Shyue [27], is a model shock-contact problem that involves the interaction of a shock wave in molybdenum and an encapsulated MORB (Mid-Ocean Ridge Basalt) liquid. The EOS coefficients of molybdenum and MORB are $(\Gamma_0,\rho_0,c_0,s)=(2.56,9.961,4.77,1.43)$ and $(\Gamma_0,\rho_0,c_0,s)=(1.18,2.66,2.1,1.68)$, respectively. The initial condition is

$$(\rho,u,p)=\begin{cases}(11.042,0.543,30) & \text{if } 0<x<0.6\\ (2.66,0,0) & \text{if } 1>x>0.6\end{cases} \tag{35}$$

and the final time is $t=0.12$. Case IV-C is problem of two Aluminum plate colliding in a vacuum. The EOS coefficients of the Aluminum plate is $(\Gamma_0,\rho_0,c_0,s)=(3,2.785,5.238,1.338)$. The initial condition is

$$(\rho,u,p)=\begin{cases}(0,0,0) & \text{if } 0<x<0.2\\ (2.785,1,0) & \text{if } 0.2<x<0.5\\ (2.785,-1,0) & \text{if } 0.8>x>0.5\\ (0,0,0) & \text{if } 1>x>0.8\end{cases} \tag{36}$$

and the final time is $t=0.1$.

Fig. 5 shows the computed velocity and density profiles. A good agreement between the numerical and the reference solution is observed. Note that for Case IV-A and Case IV-B besides of sharp interfaces, the present results have considerable better accuracy than previous results (see Figs. 5 and 6 and in Shyue [27]), especially for the smooth-solution regions. This can be expected since the present method allows to use high-order discretizations, such as the anti-diffusion 5th order WENO-LLF scheme employed in this paper, as underlying scheme.

3.5. Underwater-explosion problem

We consider a two-dimensional underwater-explosion problem. This problem has been previously simulated by Grove and Manikoff [10], Shyue [28] with a sharp-interface method: an underwater cylindrical bubble of gaseous explosive products expands and drives the air–water interface. For this case, the initial condition is

$$\begin{cases}(\rho=1.2\times10^{-3},u=0,v=0,p=1,\gamma=1.4) & \text{air}\\ (\rho=1,u=0,v=0,p=1,\gamma=7.15) & \text{water}\\ (\rho=1.25\times10^{-3},u=0,v=0,p=10^4,\gamma=1.4) & \text{gaseous bubble}\\ \phi=1.5-y & y>1.35\\ \phi=\sqrt{(x-2)^2+(y-1.2)^2}-0.12 & \text{the rest region}\end{cases}, \tag{37}$$

where the level set $\phi>0$ represents water described by a stiff gas EOS, i.e. $(\gamma-1)\rho e=p+\gamma p_0$ where $\gamma=4.4$ and $p_0=6.0\times10^3$, and $\phi\leqslant 0$ represents air and the gaseous explosive products described by an ideal-gas EOS. Initial configuration is an underwater gaseous bubble of radius 0.12 at (2,1.2) and the air–water interface at $y=1.35$ in a rectangular domain $[0,4]\times[0,2.5]$. The dimensional references are given by the state of water at 1 atmosphere and 1 m. The boundary conditions employed in the current computations are a solid-wall boundary on the bottom and an outflow boundary with zero gradient on the remaining sides. This case has been computed on a 400×250 grid, which is the same as that in Shyue [28], with the TR solver and M-HLLC solver, respectively.

Fig. 6 shows the Schlieren-type images of density and pressure calculated by the M-HLLC solver at three different times t = 0.2, 0.4 and 1.2 ms, which have no notable difference from the results obtained by the TR solver (not shown here), and are in quite good agreement with the results of Shyue [28] (their Fig. 9). In comparison to the latter more details of the reflected waves from the water-air surface are captured. The computed interface positions at three time instances are shown in Fig. 7(a). Note that, since a conservative method [14] is used, the total mass of the explosive products is conserved. Fig. 7(b) gives the pressure and density profile at $t=0.2,1.2$ ms and $x=2$. In contrast to the results obtained by Shyue [28] (their Fig. 11) with the same resolution the present method predicts sharper density and pressure profiles, especially inside the bubble, and considerably smaller undershoots of density near the material interface.

The performance analysis shows that the TR solver and the M-HLLC solver take about 0.24% and 0.05% of the total computational time. Note that, since the calculation of interface condition is carried out only on a small fraction of total grid points, the overall gain is about 6%. However, one should keep in mind that for complex interface evolution the fraction of grid points involved in the interface calculation may increase dramatically so that the overall gain can be significant.

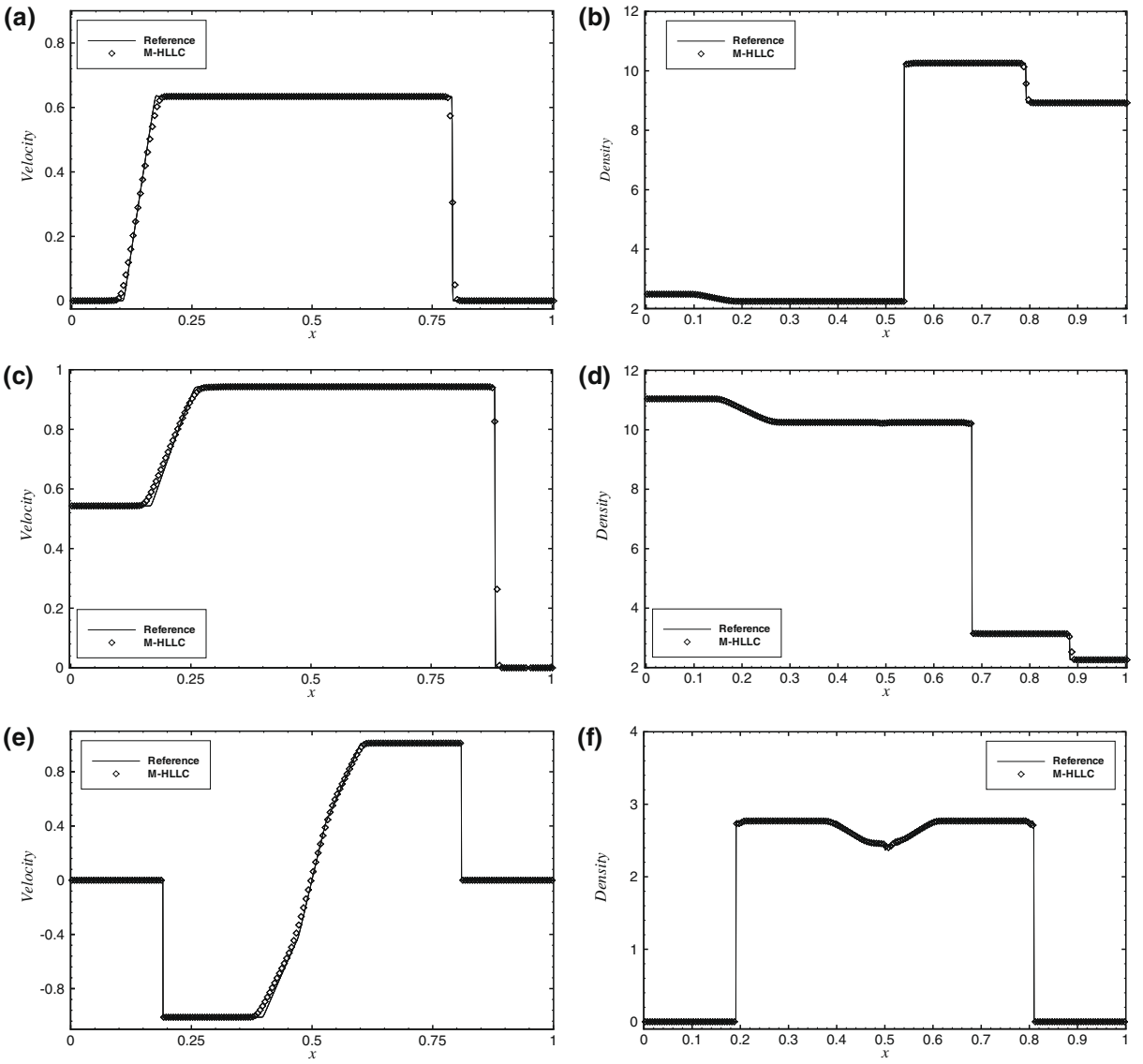

Fig. 5. Explosion and high-speed impact: Case IV-A (a) and (b); Case IV-B (c) and (d); Case IV-C (e) and (f).

3.6. Shock-contact problem in condensed materials

We consider a shock-contact problem which is a two-dimensional extension of Case IV-B, and has been studied by Miller and Puckett [20] and Shyue [27] with an interface-capturing method and by Shyue [28] with a sharp-interface method, in which a shock wave in molybdenum interacts with a region of encapsulated MORB liquid. For this case, the initial condition is

$$\begin{cases} (\rho = 9.961, u = 0, v = 0, p = 0) & \text{pre-shock molybdenum} \\ (\rho = 11.042, u = 0.543, v = 0, p = 30) & \text{post-shock molybdenum} \\ (\rho = 2.26, u = 0, v = 0, p = 0) & \text{MORB liquid} \\ \phi = -\min(|x-0.4|, |x-0.7|, |y-0.5|) & \text{if } 0.4 < x < 0.7 \text{ and } y < 0.5\,, \\ \phi = \begin{cases} |x-0.4| & \text{if } y < -1.25x + 1 \\ |x-0.7| & \text{if } y < \frac{5}{3}(x-0.7) + 0.5 \\ |y-0.5| & \text{else} \end{cases} & \text{the rest region} \end{cases} \tag{38}$$

where the level set $\phi > 0$ represents molybdenum, and $\phi \leqslant 0$ represents MORB liquid. In a unit square computational domain a planar rightward-moving Mach 1.163 shock wave in molybdenum at $x = 0.35$ travels from left to right, and a rectangular

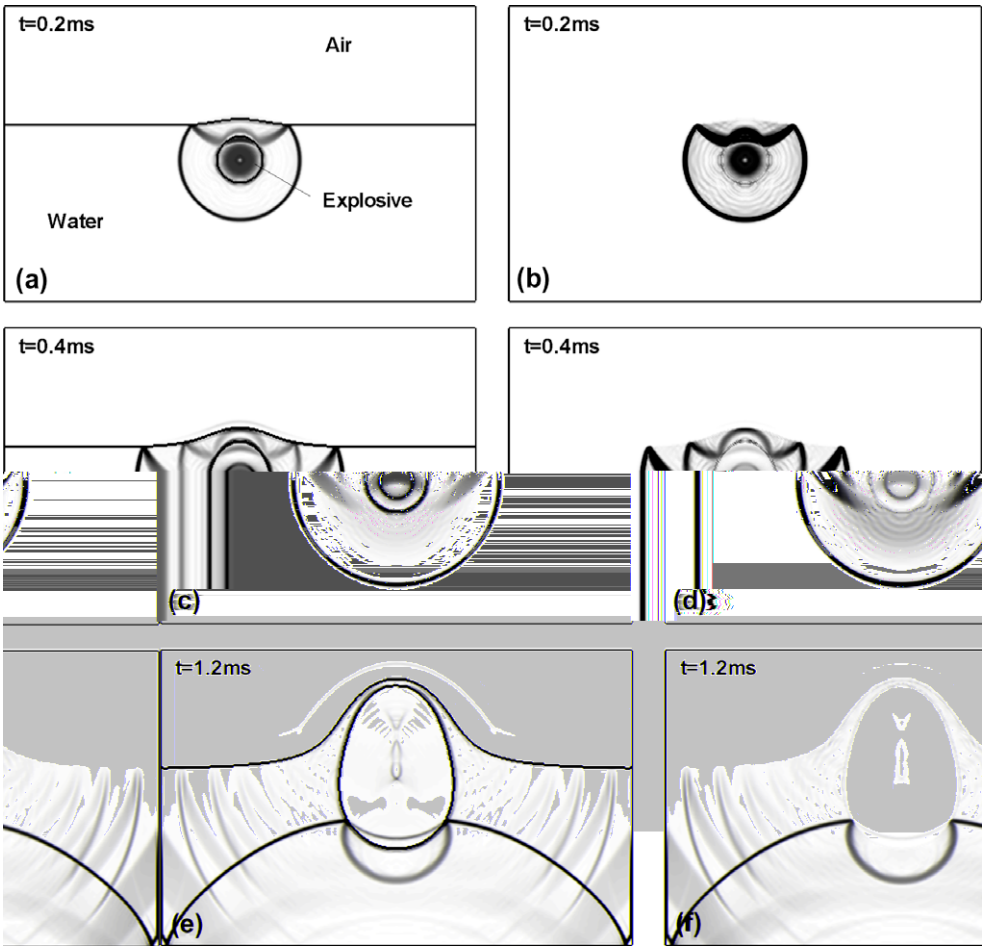

Fig. 6. Underwater-explosion problem: Schlieren-type image for (left) density and (right) pressure at three times $t = 0.2, 0.4$ and 1.2 ms.

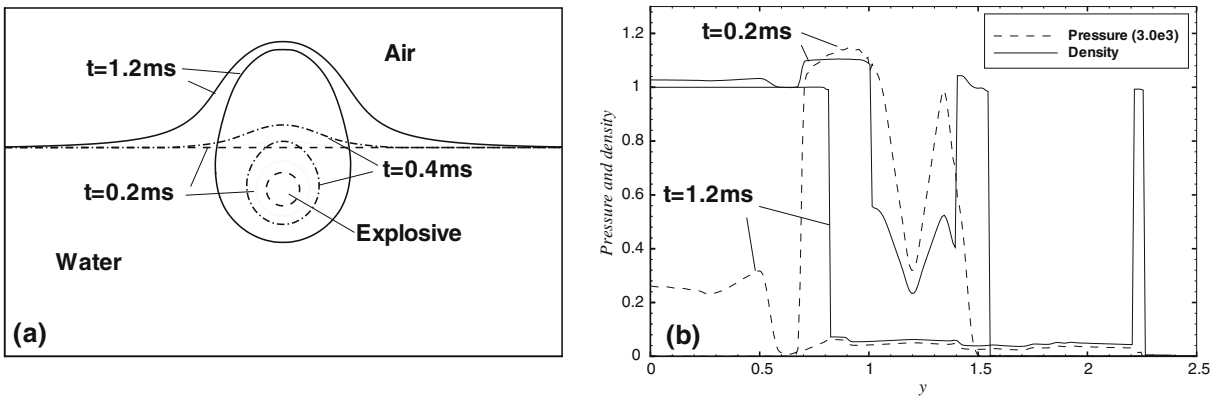

Fig. 7. Underwater-explosion problem: (a) interface positions at $t = 0$ (dashed), 0.2, 0.4 and 1.2 ms; (b) pressure and density profiles along $x = 2$ at $t = 0.2$ and 1.2 ms.

region $[0.4, 0.7] \times [0, 0.5]$ of MORB liquid in front of the shock. The dimensional reference values are 1000 kg/m^3, 1 GPa and 1 m. The boundary conditions employed in the current computations are a solid-wall boundary on the bottom, an inflow boundary on the left side, and an outflow boundary with zero gradient on the remaining sides. The computation has been carried out on a 200×200 grid, which is the same as that in Shyue [28].

Fig. 8 shows the Schlieren-type images of density and pressure calculated by the M-HLLC solver at times $t = 50$ and 100 μs, which are in quite good agreement with the results of Shyue [28] (their Fig. 12). One can find that the present results

predict a considerably smoother pressure in the region around the left-top part of the material interface, which can be further verified by the high-resolution results obtained by an interface-capturing method [29] (see also Fig. 12 in Shyue [28]). Note that there are well resolved small ripple waves originating from the left-top corner of the material interface, similar to those in Shyue [28] (see their Fig. 12(b)). They can be explained by the sound-mode interface instability which is characterized by compressibility effects. The computed interface positions at two time instances are shown in Fig. 9(a), in which a high-speed jet has developed at $t = 100$ μs. The formation of this jet can also be verified by the high-resolution results [29] (see also Fig. 12 of Shyue [28]), but is not predicted by the results in Shyue [28] (their Fig. 14) computed on the same grid. Fig. 9(b) gives the pressure and density profile at $t = 50$ and 100 μs and $y = 0.4$. Note the slight oscillations corresponding to the small ripple waves as shown in Fig. 9(b) and (d). In comparison with the pressure fronts at the reflected and transmitted waves in Shyue [28] with the same resolution (see their Fig. 13), the present method predicts sharper pressure profiles, and, considerably smaller undershoots of density near the material interface.

3.7. Shock and water-column interaction problem

We consider two cases of shock and water-column interaction problem. These cases have been simulated previously by Chang and Liou [5] with an interface-capturing method. In the first case, a water column in air is driven by a planar Mach 3 shock wave. The initial data are

$$\begin{cases} (\rho = 1.2, u = 0, v = 0, p = 1, \gamma = 1.4) & \text{pre-shocked air} \\ (\rho = 4.628, u = 2.4, v = 0, p = 10.33, \gamma = 1.4) & \text{post-shocked air} \\ (\rho = 1 \times 10^3, u = 0, v = 0, p = 1, \gamma = 7.15) & \text{water column} \\ \phi = -0.175 + \sqrt{(x - 0.55)^2 + y^2} & \text{level set} \end{cases}, \tag{39}$$

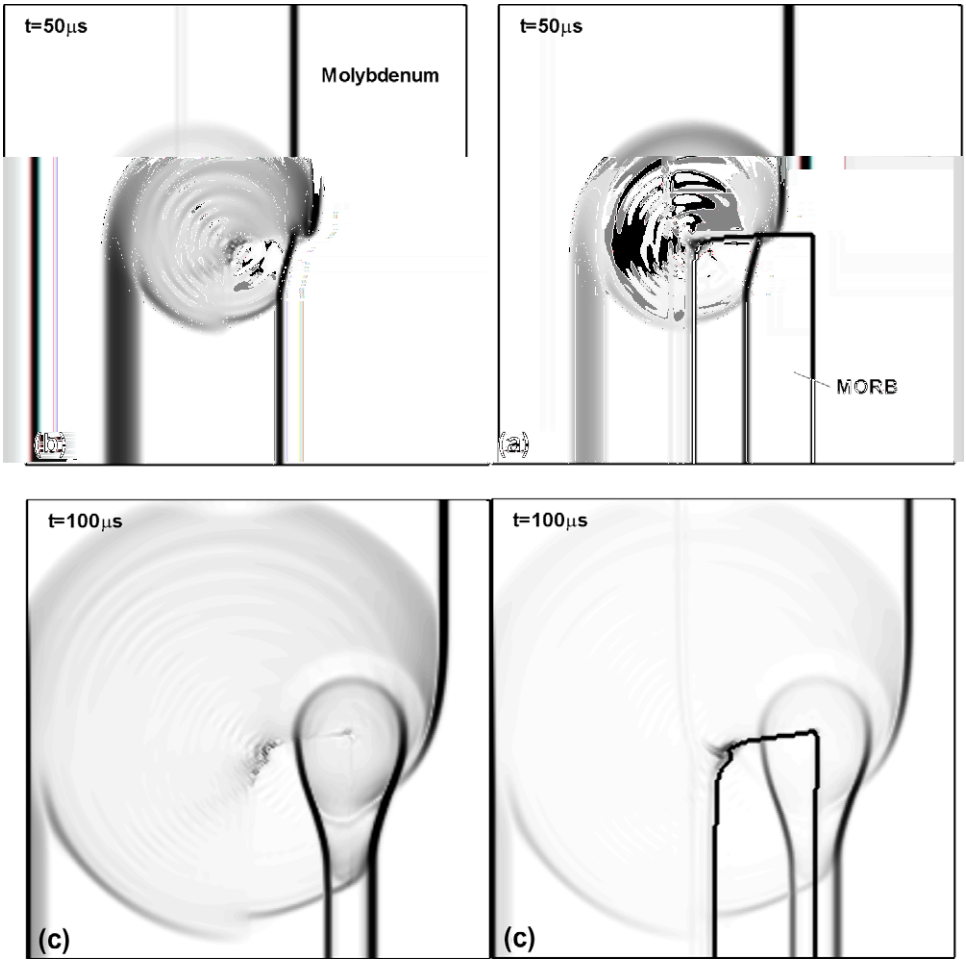

Fig. 8. Shock-contact problem in condensed materials: Schlieren-type image for (left) density and (right) pressure at three times $t = 50$ and 100 μs.

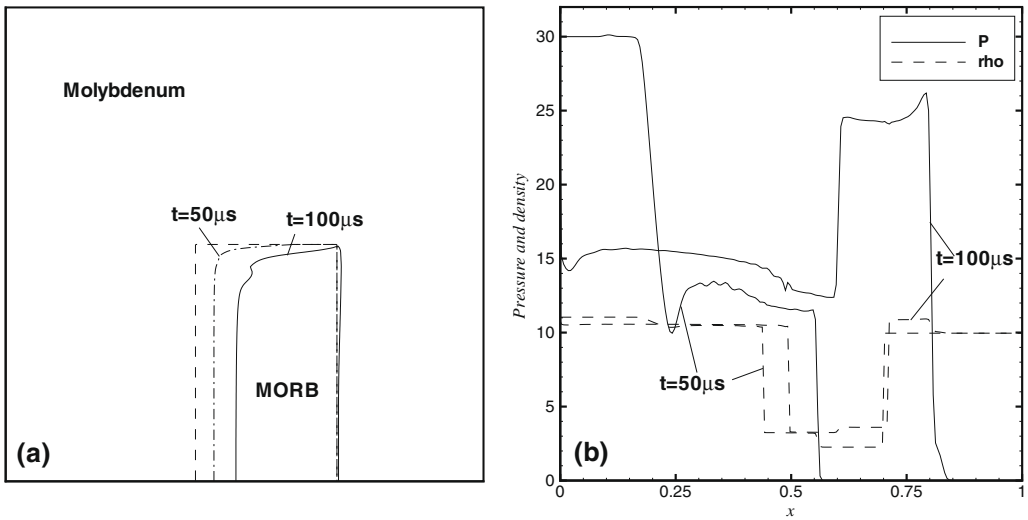

Fig. 9. Shock-contact problem in condensed materials: (a) interface positions at $t = 0$ (dashed), 50 and 100 μs; (b) pressure and density profiles along $y = 0.4$ at $t = 50$ and 100 μs.

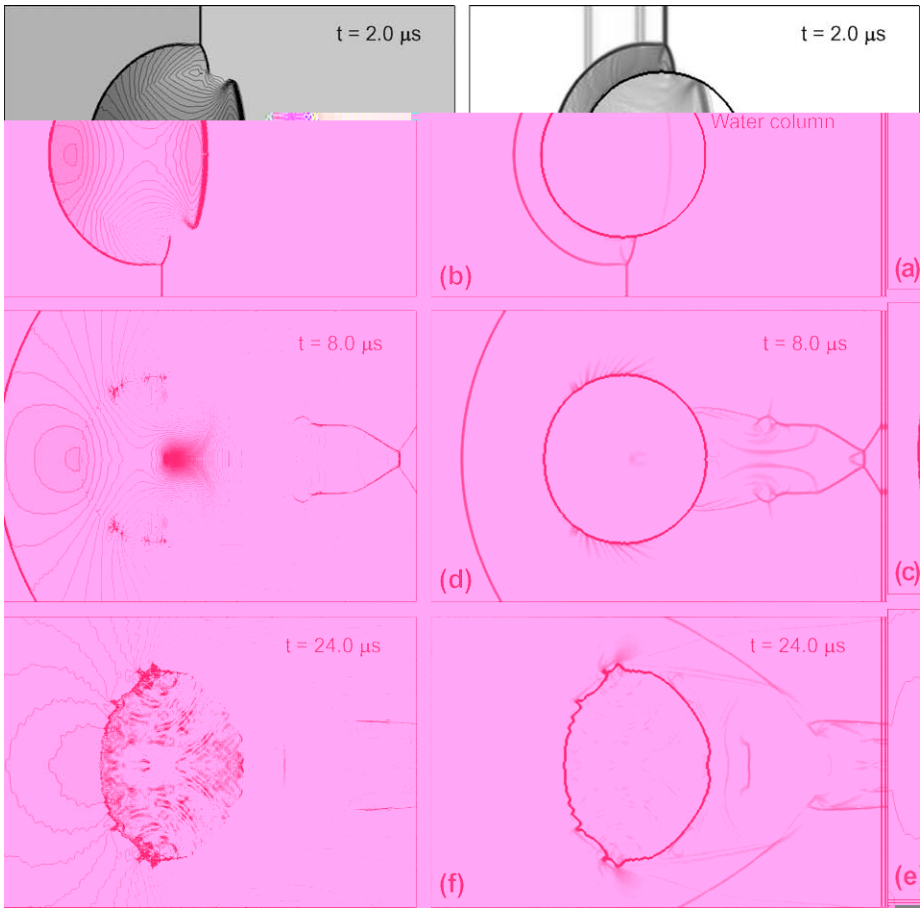

Fig. 10. Shock interacting with a water column at $t = 2.0, 8.0$ and 24.0 μs: (left) 55 contours of pressure, from −20 to 70 atm; (right) Schlieren-type image for density.

where the level set $\phi < 0$ represents the water described by Tait's EOS, and $\phi \geqslant 0$ represents the air described by an ideal-gas EOS. The initial configuration is a water column of radius 0.175 at (0.55,0.0) and a planar rightward-moving Mach 3 shock wave at $x = 0.35$ in a rectangular domain $[0, 1.2] \times [-0.7, 0.7]$. The dimensional references are given by 1 atmosphere, 1 kg/m^3 and 1 cm. The boundary conditions employed in the current computations are a solid-wall boundary on the top and bottom sides, an inflow boundary on the left side and an outflow boundary with zero gradient on the right side. The computation has been carried out on a 480×560 equidistant grid.

Fig. 10 shows the pressure contours and Schlieren-type images of density calculated by the M-HLLC solver at times $t = 2$, 8 and 24 μs, representing the early, intermediate and later stages. At the early stage, the present results are in quite good agreement with those in Chang and Liou [5] (their Fig. 14(b)). The shock wave in the air diffracts around the water column just like around a solid cylinder, the transmitted shock wave in the water is weak and travels faster than that in the air, and the pressure contours pass the air–water interface smoothly. At the intermediate stage, though the computed flow field in air is still in good agreement, more features (compared to Fig. 14(f) in Chang and Liou [5]) are predicted behind the water column by the present method. Furthermore, the present results show slightly different wave patterns in the water column and indicates that the first collapse is close to the column center. It appears that the present simulation is able to capture compressible interface instabilities. The sound mode produces ripple-like waves, bouncing back and forth between the primary bow shock and the water column, and pressure disturbances at the interface. The shear mode is not strong due to the large density ratio. Note that, due to quite different interface models, the present results for the later stages are different from those in Chang and Liou [5]. Fig. 10(e) and (f) shows that wrinkles are produced at the positions where the interface instabilities originate. Consequently, these wrinkles intensify the ripple-like waves and introduce tiny separation regions behind. After being reflected several times back and forth ar the front and rear interfaces, the waves in the water column produce a very complicated pattern with regions characterized by positive and negative pressures.

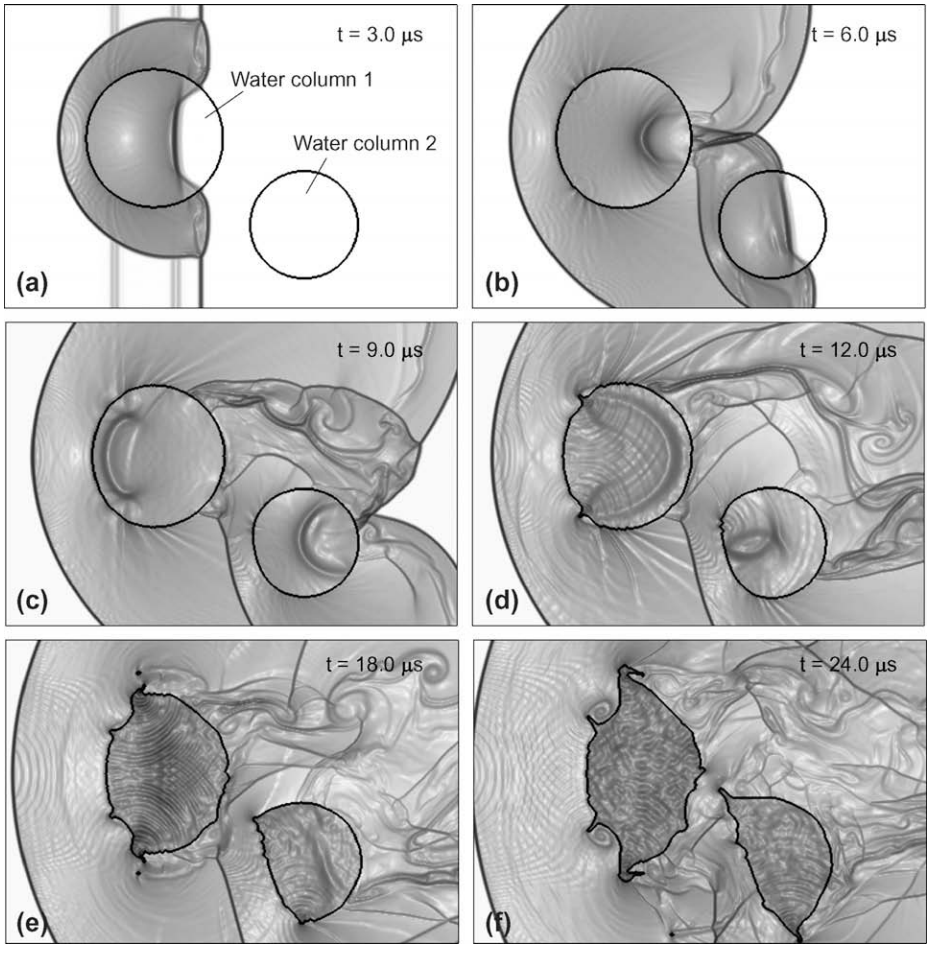

Fig. 11. Shock interacting with two water columns: Schlieren-type image for density at $t = 3.0, 6.0, 9.0, 12.018.0$ and 24.0 μs.

In the second case, two different-size water columns in air are driven by a planar Mach 6 shock wave. The initial data are

$$\begin{cases} (\rho = 1, u = 0, v = 0, p = 1, \gamma = 1.4) & \text{pre-shocked air} \\ (\rho = 6.32, u = 5.25, v = 0, p = 41.84, \gamma = 1.4) & \text{post-shocked air} \\ (\rho = 1 \times 10^3, u = 0, v = 0, p = 1, \gamma = 7.15) & \text{water column} \\ \phi = -0.32 + \sqrt{(x-0.8)^2 + (y-1.4)^2} & \text{level set for } y > x + 0.05 \\ \phi = -0.25 + \sqrt{(x-1.5)^2 + (y-1)^2} & \text{level set for the rest region} \end{cases}, \tag{40}$$

where the level set $\phi < 0$ represents the water and $\phi \geqslant 0$ represents the air. The initial configuration consist of two water columns of radius 0.32 and 0.25 at (0.8, 1.4) and (1.5, 1), respectively, and a planar rightward-moving Mach 6 shock wave at $x = 0.4$ in a rectangular domain $[0, 2.4] \times [0, 2.8]$. The same EOS, dimensional references and boundary conditions as in the first case are used. The computation has been carried out on a 480×560 grid.

Fig. 11 shows Schlieren-type images of density calculated by the M-HLLC solver at times t = 3, 6, 9, 12, 18 and 24 μs. Note that the present method does not result in negative gas pressure as in Chang and Liou [5], and allows for continuing the calculation beyond 13 μs. Different from the first case, the transmitted shock wave here is slower than the shock wave in the air (see Fig. 11(a)). Other than introducing a collapse inside the water column as in the first case, the low pressure region moves towards the front side (see Fig. 11(c)), collapses there and immediately produces another rarefaction wave which moves back to the rear side (see Fig. 11(d)). Meanwhile, as interface instabilities develop, two wrinkles are produced at water column 1 and one wrinkle is produced at water column 2 (see Fig. 11(d)). It is interesting to note that, though our results show quite different wave patterns within the water columns compared with those in Chang and Liou [5], similar interface features occur at almost the same corresponding positions, e.g. wrinkles can be found in their results too (see their Fig. 14(e)). These wrinkles grow gradually and eject small water drops (see Fig. 11(e)). Due to interface instabilities, more wrinkles are produced (see Fig.11(f)), and eventually eject more water drops.

4. Concluding remarks

In this paper, we have proposed a sharp-interface interaction method based on the HLLC Riemann solver. Interface conditions have been formulated for general compressible multi-fluid flows. Interfacial states are obtained by a one-step method without root-finding or iteration, which makes the method suitable for interactions involving general equations of state and material interfaces. A number of numerical examples in one dimension is provided for comparison with exact solutions and results from an iterative interface interaction solver. Two dimensional problems are calculated and compared to results of previous works. The obtained results suggest that the Riemann solver exhibits superior robustness and comparable accuracy as previous iterative solvers while being significantly more efficient. Though originally being proposed for the sharp-interface method, since no specific properties of the underlying discretization scheme or interface reconstruction are required, the present solver may also be applied to other numerical schemes and interface-capturing methods. The application of the single-phase Roe average to other numerical methods, which use characteristic decomposition or approximate Riemann solvers, is straightforward. It is applied, e.g. in this paper, with the characteristic WENO scheme as single-phase solver. The multi-fluid solver can also be applied to the interface-capturing methods, such as that of Chang and Liou [5], in which Riemann problems between different fluids need to be solved.

Acknowledgment

Part of the work has been done during the visit of the first author at the CTR summer program 2008 at Stanford University.

Appendix A. Conservative interface method

In Hu et al. [14], the conservative interface method is formulated following the standard finite volume approach. Considering Eq. (1) for the fluid occupying the sub-domain Ω^1 on a two-dimensional Cartesian grid with grid spacings Δx and Δy, a finite volume discretization can be obtained from integrating Eq. (1) over the space-time volume $\Delta_{ij} \bigcap \Omega^1(t)$ of a computational cell (i,j) occupied by the fluid

$$\int_n^{n+1} dt \int_{\Delta_{ij} \bigcap \Omega^1(t)} dxdy \left(\frac{\partial \mathbf{U}}{\partial t} + \nabla \cdot \mathbf{F} \right) = 0, \tag{A.1}$$

where $\Delta_{ij} = \Delta x \Delta y$ is the cell volume. $\Delta_{ij} \bigcap \Omega^1(t)$ can be represented by $\alpha_{i,j}(t) \Delta x \Delta y$ where $\alpha_{i,j}(t)$ is the time dependent volume fraction of the considered fluid and satisfying $1 \geqslant \alpha \geqslant 0$. By an application of Gauss's theorem, one obtains

$$\int_n^{n+1} dt \int_{\Delta_{ij} ap \Omega^1(t)} dxdy \frac{\partial \mathbf{U}}{\partial t} + \int_n^{n+1} dt \int_{\partial(\Delta_{ij} \bigcap \Omega^1(t))} dxdy \mathbf{F} \cdot \mathbf{n} = 0 \tag{A.2}$$

where $\partial\Delta_{ij}$ are the four cell faces intersecting vertically with the grid at four locations $(x_i+\Delta x/2, y_j), (x_i, y_j+\Delta y/2), (x_i-\Delta x/2, y_j)$ and $(x_i, y_j-\Delta y/2)$. Denoting the interface location as $\Gamma(t)$, as shown in Fig. A.1, $\partial(\Delta_{ij}\bigcap\Omega^1(t))$ can be represented by two parts: one is the combination of the four segments of the cell faces being cut by the interface, which can be written in the form $A_{i+1/2,j}(t)\Delta y, A_{i,j+1/2}(t)\Delta x, A_{i-1/2,j}(t)\Delta y$ and $A_{i,j-1/2}(t)\Delta x$, where $1 \geqslant A \geqslant 0$ is cell-face aperture; the other one is the segment of the interface $\Delta\Gamma_{i,j}(t)$ inside of the cell (i,j). Hence, Eq. (A.2) can be rewritten as

$$\alpha_{i,j}^{n+1}\mathbf{U}_{i,j}^{n+1} = \alpha_{i,j}^{n}\mathbf{U}_{i,j}^{n} + \int_n^{n+1} dt\frac{1}{\Delta x\Delta y}\widehat{\mathbf{X}}[\Gamma_{i,j}(t)] + \int_n^{n+1} dt\frac{1}{\Delta x}[A_{i+1/2,j}(t)\widehat{\mathbf{F}}_{i+1/2,j} - A_{i-1/2,j}(t)\widehat{\mathbf{F}}_{i-1/2,j}] + \int_n^{n+1} dt\frac{1}{\Delta y}[A_{i,j+1/2}(t)\widehat{\mathbf{F}}_{i,j+1/2} - A_{i,j-1/2}(t)\widehat{\mathbf{F}}_{i,j-1/2}] \tag{A.3}$$

where $\alpha_{i,j}(t)\mathbf{U}_{i,j}$ and $\mathbf{U}_{i,j}$ are the conservative quantities in the cut cell and the cell-averaged density of conservative quantities of the considered fluid, respectively. $\widehat{\mathbf{F}}$ is the cell-face flux, which is obtained by standard high-order shock-capturing schemes, e.g. WENO scheme [15], and $\widehat{\mathbf{X}}[\Gamma_{i,j}(t)]$ is the momentum and energy exchange across the interface segment determined by the interface interaction of Eq. (2). With explicit first-order forward time difference (show here for simplicity), the above equation can be approximated as

$$\alpha_{i,j}^{n+1}\mathbf{U}_{i,j}^{n+1} = \alpha_{i,j}^{n}\mathbf{U}_{i,j}^{n}\frac{\Delta t}{\Delta x\Delta y} + \widehat{\mathbf{X}}(\Delta\Gamma_{i,j}) + \frac{\Delta t}{\Delta x}[A_{i-1/2,j}\widehat{\mathbf{F}}_{i-1/2,j} - A_{i+1/2,j}\widehat{\mathbf{F}}_{i+1/2,j}] + \frac{\Delta t}{\Delta y}[A_{i,j-1/2}\widehat{\mathbf{F}}_{i,j-1/2} - A_{i,j+1/2}\widehat{\mathbf{F}}_{i,j+1/2}] \tag{A.4}$$

where Δt is the time step size. Note that all the terms on the right-hand-side are evaluated at time step n. It can be found that global conservation for the considered fluid is satisfied by summing Eq. (A.4) over the entire domain

$$\sum_{i,j}\alpha_{i,j}^{n+1}\mathbf{U}_{i,j}^{n+1} = \sum_{i,j}\alpha_{i,j}^{n}\mathbf{U}_{i,j}^{n} + \sum_{i,j}\frac{\Delta t}{\Delta x\Delta y}\widehat{\mathbf{X}}(\Delta\Gamma_{i,j}) + \text{boundary terms} \tag{A.5}$$

where the interface-exchange term (second term on right-hand-side) vanishes in all full cells. Note that for two-fluid problems, the evolution of each fluid is computed by solving Eq. (A.4) where the interface-exchange term has opposite sign. Therefore, overall conservation can be achieved by summing Eq. (A.5) for the two fluids

$$\sum_{k=1,2}\sum_{i,j}\alpha_{i,j}^{n+1}\mathbf{U}_{i,j}^{n+1} = \sum_{k=1,2}\sum_{i,j}\alpha_{i,j}^{n}\mathbf{U}_{i,j}^{n} + \text{boundary terms}. \tag{A.6}$$

Note that a Runge–Kutta scheme can be employed for higher order time integration while maintaining discrete conservation since every Runge–Kutta sub-step can be formulated as Eq. (A.4).

A.1. Interface description

Associating the computational domain Ω with a signed distance function $\phi(x,y,t)$, i.e. the level set function [22], the interface can be located by finding the zero level set of ϕ. It can be found that the continuous updating of ϕ is equivalent to the advection of the interface [30] by the equation

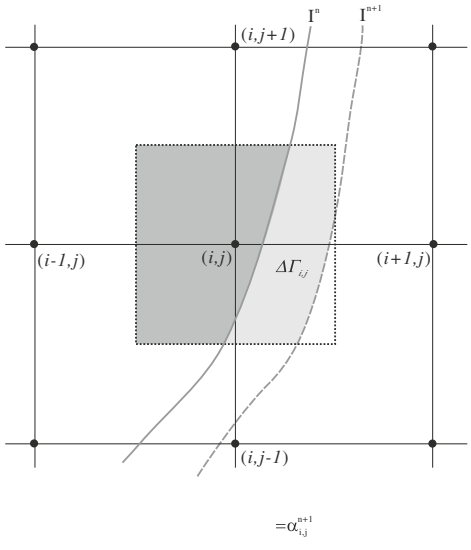

$$\phi_t + \mathbf{v}\cdot\nabla\phi = 0 \tag{A.7}$$

where $\mathbf{v}$ is the advection velocity of the level sets. In practice, the level sets are only updated in the near interface region, which usually includes the first and second nearest cell-layers. For the region far from the interface the level sets are re-initialized [30] by the equation

$$\phi_\tau + \mathrm{sgn}(\phi)(|\nabla\phi| - 1) = 0, \tag{A.8}$$

where $\mathrm{sgn}(\phi)$ is a sign function, to maintain the signed distance property of level set function.

A.2. Interface reconstruction

The cell-face apertures are calculated by assuming a linear distribution of the level set along the cell face. By including the information on the level set normal direction a prediction of the two-dimensional volume fraction can be given as

$$H(\phi,\varepsilon) = \begin{cases} 0 & \text{if } \Lambda > \Gamma, \quad \phi < 0 \\ \frac{1}{2} + \frac{1}{\varepsilon^2} D\phi + \frac{1}{2}\frac{\Lambda^2}{\varepsilon\Gamma} & \text{if } \Gamma \geqslant \Lambda \geqslant 0, \quad \phi < 0 \\ \frac{1}{2} + \frac{1}{\varepsilon^2} D\phi & \text{if } \Lambda < 0 \\ \frac{1}{2} + \frac{1}{\varepsilon^2} D\phi - \frac{1}{2}\frac{\Lambda^2}{\varepsilon\Gamma} & \text{if } \Gamma \geqslant \Lambda \geqslant 0, \quad \phi > 0 \\ 1 & \text{if } \Lambda > \Gamma, \quad \phi > 0 \end{cases} \tag{A.9}$$

in which $D = \varepsilon \min\left(\frac{1}{|N_x|}, \frac{1}{|N_y|}\right)$, $\Gamma = \sqrt{D^2 - \varepsilon^2}$ and $\Lambda = \frac{\Gamma}{2} + \frac{D|\phi|}{\varepsilon} - \frac{\varepsilon}{2}$. The above smoothed Heaviside functions are symmetric to $\phi = 0$ returning a volume fraction of 0.5. For a given fluid all the cells can be classified into three types: cells with volume fraction larger than 0.5 are normal cells, cells with volume fraction less than 0.5 but non-zero are small cells, and otherwise they are empty cells.

A.3. A mixing procedure

For a small or empty cell, a stable fluid state may not be obtained based on the time step calculated according to the full grid size CFL condition. Therefore, it is suggested that the fluid in those cells is mixed with that of their neighboring cells. As the targeted neighboring cells are preferably are normal cells, they are determined from the level set normal direction.

The changes of the conservative quantities in the x and y directions for the small cells and the targeted cells after a mixing operation are calculated according to the averaged conservative quantities. Then the conservative quantities for one fluid in the near interface cells are updated by

$$\alpha_{i,j}^{n+1}\mathbf{U}_{i,j}^{n+1} = (\alpha_{i,j}^{n+1}\mathbf{U}_{i,j}^{n+1})^* + \sum_k \mathbf{M}^x + \sum_l \mathbf{M}^y \tag{A.10}$$

where $(\alpha_{i,j}^{n+1}\mathbf{U}_{i,j}^{n+1})^*$ are the conservative quantities at time step $n+1$ before mixing. Here, the second and third terms on the right hand side are the summations taken for all the mixing operations in the x and y directions, respectively. Note that the present mixing procedure treats vanished and newly created empty cell automatically. For the former case, the residual conservative quantities are all transported to target cells and, for the latter case all the conservative quantities in a newly created small cell are transported from its target cells.

A.4. Interface exchanges

To obtain the momentum and energy exchanges across the interface, the proposed Riemann problems associated with interface interactions are solved on the grid points within near interface region band along the interface normal direction. After the interface interaction has been solved the interface pressure p_I and the normal velocity $\mathbf{v}_I \equiv (u_I, v_I)$ are obtained. Hence, for the fluid corresponding to $\phi > 0$, the momentum and energy transferred to it are

$$\widehat{\mathbf{X}}^{\mathbf{P}}(\Delta\Gamma) = p_I\Delta\Gamma\mathbf{N}_I \quad \text{and} \quad \widehat{X}^E(\Delta\Gamma) = p_I\Delta\Gamma\mathbf{N}_I\cdot\mathbf{v}_I, \tag{A.11}$$

respectively. Here $\Delta\Gamma$ and $\mathbf{N}_I$ are the interface segment length or area and normal direction, respectively. $\widehat{\mathbf{X}}^{\mathbf{P}} = (\widehat{X}_x^{\mathbf{P}}, \widehat{X}_y^{\mathbf{P}})$ stands for the transferred momentum in the respective x and y directions and $\widehat{X}^E$ stands for the transferred energy. Note that there is no exchange of the tangential momentum and energy, which recovers exact discontinuities of tangential velocity on the interface.

Appendix B. Borges's anti-diffusion technique for 5th-order WENO scheme

In Borges's version of 5th-order WENO scheme [4], the non-oscillatory weights are obtained by

$$\alpha_k = d_k\left[1 + \left(\frac{\tau_5}{\beta_k + \epsilon}\right)\right], \quad k = 0,1,2. \tag{B.1}$$

where d_k are idea weights and β_k are the classical kth smoothness indicators of 3rd-order stencils

$$\begin{aligned}
\beta_0 &= \frac{1}{4}(f_{i-2} - 4f_{i-1} + 3f_i)^2 + \frac{13}{12}(f_{i-2} - 2f_{i-1} + f_i)^2,\\
\beta_1 &= \frac{1}{4}(f_{i-1} - f_{i+1})^2 + \frac{13}{12}(f_{i-1} - 2f_i + f_{i+1})^2,\\
\beta_2 &= \frac{1}{4}(3f_i - 4f_{i+1} + f_{i+2})^2 + \frac{13}{12}(f_i - 2f_{i+1} + f_{i+2})^2,
\end{aligned} \tag{B.2}$$

in which $f_{i+l}, l = -2, \ldots, 2$, are the underlying numerical fluxes, i.e. the Lax-Friedrichs fluxes, calculated with the cell-average values. $\tau_5 = |\beta_0 - \beta_2|$ in Eq. (B.1) gives a higher-order smoothness indicator. This scheme decreases the dissipation considerably because Eq. (B.1) assigns substantially larger weights to less smooth stencils than the original WENO scheme [15].

References

[1] R. Abgrall, S. Karni, Computations of compressible multifluids, J. Comput. Phys. 169 (2001) 594–623.
[2] G.J. Ball, B.P. Howell, T.G. Leighton, M.J. Schofield, Shock induced collapse of a cylinder air cavity in water: a free Lagrange simulation, Shock Waves 10 (2000) 265–276.
[3] P. Batten, N. Clarke, C. Lambert, D.M. Causon, On the choice of wavespeeds for the HLLC Riemann solver, SIAM J. Sci. Comput. 18 (1997) 1553–1570.
[4] R. Borges, M. Carmona, B. Costa, W.S. Don, An improved weighted essentially non-oscillatory scheme for hyperbolic conservation laws, J. Comput. Phys. 227 (2008) 3191–3211.
[5] C.H. Chang, M.S. Liou, A robust and accurate approach to computing compressible multiphase flow: stratified flow model and AUSM$^+$-up scheme, J. Comput. Phys. 225 (2007) 840–873.
[6] B. Einfeldt, C.D. Munz, P.L. Roe, B. Sjögreen, On Godunov-type methods near low densities, J. Comput. Phys. 92 (1991) 273–295.
[7] R. Fedkiw, T. Aslam, B. Merriman, S. Osher, A non-oscillatory Eulerian approach to interfaces in multimaterial flows (the ghost fluid method), J. Comput. Phys. 152 (1999) 457–492.
[8] P. Glaister, An approximate linearised Riemann solver for the Euler equation for real gases, J. Comput. Phys. 74 (1988) 382–408.
[9] J. Glimm, D. Marchesin, O. McBryan, A numerical method for two phase flow with an unstable interface, J. Comput. Phys. 39 (1981) 179–200.
[10] J. Grove, R. Manikoff, Anomalous reflection of shock wave at a fluid interface, J. Fluid Mech. 219 (1990) 313–336.
[11] A. Harten, P.D. Lax, B. van Leer, On upstream differencing and Godunov-type schemes for hyperbolic conservation laws, SIAM Rev. 25 (1983) 35–61.
[12] C.W. Hirt, B.D. Nichols, Volume of fluid (VOF) method for the dynamics of free boundaries, J. Comput. Phys. 39 (1981) 201.
[13] X.Y. Hu, B.C. Khoo, An interface interaction method for compressible multifluids, J. Comput. Phys. 198 (2004) 35–64.
[14] X.Y. Hu, B.C. Khoo, N.A. Adams, F.L. Huang, A conservative interface method for compressible flows, J. Comput. Phys. 219 (2006) 553–578.
[15] G.S. Jiang, C.W. Shu, Efficient implementation of weighted ENO schemes, J. Comput. Phys. 126 (1996) 202–228.
[16] T. Linde, A practical, general-purpose, two-state HLL Riemann solver for hyperbolic conservation laws, Int. J. Numer. Meth. Fluids 40 (2002) 391–402.
[17] T.G. Liu, B.C. Khoo, K.S. Yeo, Ghost fluid method for strong shock impacting on material interface, J. Comput. Phys. 190 (2003) 651–681.
[18] M.S. Liou, B. van Leer, J.S. Shuen, Splitting for inviscid fluxes for real gas, J. Comput. Phys. 87 (1990) 1–24.
[19] H. Luo, J.D. Baum, R. Löhner, On the computation of multi-material flows using ALE formulation, J. Comput. Phys. 194 (2004) 304–328.
[20] G.H. Miller, E.G. Puckett, A high-order Godunov method for multiple condensed phases, J. Comput. Phys 128 (1996) 134–164.
[21] L. Mottura, L. Vigevano, M. Zaccanti, An evaluation of Roe's scheme generalizations for equilibrium real gas flows, J. Comput. Phys. 138 (1997) 354–399.
[22] S. Osher, J.A. Sethain, Front propagating with curvature dependent speed: algorithm based on Hamilton–Jaccobi formulation, J. Comput. Phys. 79 (1988) 12–49.
[23] P.L. Roe, Approximate Riemann solvers, parameter vectors and difference schemes, J. Comput. Phys. 43 (1981) 357–372.
[24] G. Rudinger, Wave Diagrams for Nonsteady Flow in Ducts, Dover, New York, 1969.
[25] R. Saurel, R. Abgrall, A multiphase godunov method for compressbile multifluid and multiphase flows, J. Comput. Phys. 150 (2) (1999) 425–467.
[26] C.W. Shu, S. Osher, Efficient implementation of essentially non-oscillatory shock-capturing schemes, J. Comput. Phys. 77 (1988) 439–471.
[27] K.M. Shyue, A fluid-mixture type algorithm for compressible multicomponent flow with Mie–Gruneisen equation of state, J. Comput. Phys. 171 (2001) 678–707.
[28] K.M. Shyue, A wave-propagation based volume tracking method for compressible multicomponent flow in two space dimensions, J. Comput. Phys. 215 (2006) 219–244.
[29] K.M. Shyue, Private Communication (2008).
[30] M. Sussman, E. Fatemi, P. Smereka, S. Osher, An improved level set method for incompressible two-phase flows, Comp. Fluids 27 (1998) 663–680.
[31] E.F. Toro, Riemann Solvers and Numerical Methods for Fluid Dynamics: A Practical Introduction, Springer, Berlin, New York, 1997.
[32] E.F. Toro, M. Spruce, M. Speares, Restoration of the contact surface in the HLL-Riemann solver, Shock Waves 4 (1994) 25–34.
[33] B. Wang, H.Q. Xu, A method based on Riemann problem in tracking multi-material interface on unstructured moving grids, Eng. Appl. Comput. Fluid Mech. 1 (2007) 325–336.
[34] P. Woodward, P. Colella, The numerical simulation of two-dimensional fluid flow with strong shocks, J. Comput. Phys. 54 (1984) 115–173.
[35] T. Yabe, F. Xiao, T. Utsumi, The constrained interpolation profile method for multiphase analysis, J. Comput. Phys. 169 (2001) 556–593.